SABER observations of the OH Meinel airglow variability near the mesopause

Daniel R. Marsh and Anne K. Smith

National Center for Atmospheric Research, Boulder, Colorado

Martin G. Mlynczak

Atmospheric Science Competency, NASA Langley Research Center, Hampton, Virginia

Short title: SABER OH AIRGLOW

Abstract. The Sounding of the Atmosphere using Broadband Emission Radiometry (SABER) instrument, one of four on board the TIMED satellite, observes the OH Meinel emission at 2.0 μm that peaks near the mesopause. The emission results from reactions between members of the oxygen and hydrogen chemical families that can be significantly affected by mesopause dynamics. In this study we compare SABER measurements of OH Meinel emission rates and temperatures with predictions from a 3-dimensional chemical dynamical model. In general, the model is capable of reproducing both the observed diurnal and seasonal OH Meinel emission variability. The results indicate that the diurnal tide has a large effect on the overall magnitude and temporal variation of the emission in low latitudes. This tidal variability is so dominant that the seasonal cycle in the nighttime emission depends very strongly on the local time of the analysis. At higher latitudes, the emission has an annual cycle that is due mainly to transport of oxygen by the seasonally reversing mean circulation.

Introduction

The mesopause region of the atmosphere (≈80-100 km) does not easily lend itself to *in situ* sampling since it is beyond the range of meteorological balloons and too low to be practically sampled by satellites. However, remote sensing of mesopause emissions from the ground or via satellite does allow investigation of the composition and dynamics of this region. Of particular interest is the emission from the excited state of hydroxyl (OH^*) in the Meinel bands. This state can be produced through the following reaction,

$$H + O_3 \rightarrow OH^* + O_2, \tag{1}$$

and peaks near 87 km in altitude during the nighttime. The intensity of a particular Meinel band depends strongly on both the distribution of the minor constituents hydrogen and ozone and, through their effects on reaction rates, on the local temperature and density. It follows that dynamically induced perturbations in minor constituents or in the background atmosphere can manifest themselves as observable changes in emission rates. Examples of this can be seen in the 'all-sky' camera observations of Meinel emissions, which routinely indicate signatures from the passage of gravity waves through the mesopause region [*Taylor et al.*, 1997]. Global scale wave effects are seen in both ground-based and satellite observations [e.g. *Hecht et al.*, 1998; *Lowe et al.*, 1996]. In addition, ground based observations of the distribution of rotational lines within a band can be used to derive temperatures and provide information on the diurnal and seasonal variability in mesopause temperatures [*Pendleton et al.*, 2000; *Phillips et al.*, 2004].

Finally, observations of hydroxyl airglow can be used to derive atomic oxygen concentrations. Near the mesopause, the concentration of ozone at night is determined by the balance between production through recombination of atomic oxygen and losses by reactions with atomic hydrogen:

$$[O_3] = \frac{k_{O+O_2+M}[O][O_2][M]}{k_{H+O_3}[H]}. \tag{2}$$

The production rate for excited OH is:

$$P = k_{H+O_3}[H][O_3], \tag{3}$$

From substitution of the $[O_3]$ in (2) into (3), it is clear that the production rate is proportional to the atomic oxygen concentration. *Russell and Lowe* [2003] used this relationship to derive a seasonal, global climatology of atomic oxygen from observations made by the Wind Imaging Interferometer (WINDII) on the Upper Atmosphere Research Satellite (UARS).

Previous studies have looked at the diurnal and seasonal variability of OH* emissions but, because of observational constraints, have been focused primarily on the low-latitudes or have not extended over the entire annual cycle. *Le Texier et al.* [1989] showed the seasonal variation of OH* emissions observed by the Solar Mesosphere Explorer (SME), but low signal-to-noise limited nighttime observations to within 20 degrees of the equator. In addition, since SME was in a sun-synchronous orbit, nighttime observations were at one local time. Results presented here indicate seasonality depends critically on the local time of observations.

A study of measurements by the UARS Improved Stratosphere and Mesosphere Sounder (ISAMS) [*Zaragoza et al.*, 2001] did present high-latitude observations, but only covered three seasons, and did not study the seasonal cycle as a function of local time. *Melo et al.* [1999] analyzed WINDII low-latitude observations for two seasons and showed good agreement with ground-based observations. Their study showed that the diurnal cycle in emissions varied significantly between equinox and solstice, which was interpreted as an effect of tidal variability.

In this paper we compare satellite observations of OH Meinel emissions to simulations from a 3-dimensional chemical-dynamical model, in order *i)* to test the current capability of models to reproduce observed diurnal and seasonal variations, and *ii)* to further investigate the processes that drive OH Meinel emission variability.

SABER observations

The SABER instrument is one of four instruments on board the Thermosphere Ionosphere Mesosphere Energetics and Dynamics (TIMED) satellite. SABER is a radiometer that observes infrared emissions that occur between 1.27μm and 15.2μm [*Mlynczak*, 1997]. This includes emissions from carbon dioxide, ozone, nitric oxide, water vapor and excited states of molecular oxygen and hydroxyl. Temperature measurements can also be obtained from the CO_2 emissions [*Mertens et al.*, 2004]. The SABER orbit is nearly sun-synchronous; i.e. observations at a particular latitude are at approximately the same local solar time. However, the orbital precession is such that the local time varies slowly from day to day; in approximately 60 days good local time coverage is obtained. This paper presents analysis of version 1.04 of SABER 2.0 μm OH Meinel and temperature observations (available via anonymous ftp from *saber.larc.nasa.gov*). OH emission data in the public next release (version 1.06) is not expected to differ significantly from the version used in this study.

Diurnal variations

SABER data from March 26 to May 19, 2002 (days 85 to 139) were binned with respect to pressure level, local time, and latitude. During this period, the instrument was oriented to look towards the south pole, and covered latitudes approximately 50°N to 80°S. By binning in local time irrespective of longitude, the effects of waves that are not sun-synchronous will be filtered out in the binning process.

The averaged vertical structure near the equator of 2.0 μm OH Meinel volume emission rate (VER) and temperature at two differing local times are shown in Figure 1. Peak emission rates are in the range of approximately 1-2 x 10^{-7} ergs cm^{-3} s^{-1}. It is generally thought that emission decreases throughout the night because of decreasing atomic oxygen concentrations [*Lowe et al.*, 1996]. However, SABER results indicate that the emission below the peak is larger in the mean profile after midnight than the one from before midnight. It will be shown later that the observed behavior is the result of large scale advection by atmospheric tides, whose signature can be seen as wave features in the temperature profiles (Figure 1b).

Figure 2 shows the vertical distribution of OH Meinel emissions and temperatures as a function of latitude at 0215 hrs. local time. It is clear that the height and magnitude of maximum emission varies significantly as a function of latitude. The temperature and emission rates appear to be correlated near and below the peak in emission (80-95 km). Temperatures in Figure 2b show structure consistent with variations induced by the first symmetric propagating diurnal tide [*Forbes*, 1982], which maximizes at the equator, and has secondary maxima near ±30° latitude. Similar temperature structure has been seen by UARS [*Yudin et al.*, 1998] and CRISTA 1 [*Ward et al.*, 1999]. Above the peak, the relationship between emission and temperature is reversed, with higher emissions occurring where temperatures are cooler.

Figure 3 shows the local time and latitude variations of airglow emissions at two different pressure levels corresponding to heights of approximately 88 and 99 km. There are several features that are present in the emission at both altitudes. First, the emission rate is significantly larger during the nighttime. Ozone concentrations are much lower in the daytime due to loss by photolysis, and so the rate of production of excited OH is far less than at night. Second, emission rates in the nighttime are highest at the equator, and have local minima at around ± 30 degrees in latitude. This latitudinal structure was also seen in the ISAMS observations during March/April 1992 [*Zaragoza et al.*, 2001]. The observed local time variation is a maximum at the equator and a minimum at 30°S a few hours before midnight. Similar variations were again seen in the ISAMS data and the equatorial equinox Atmospheric Explorer (AE) observations of *Abreu and Yee* [1989].

The changing relationship between emission rate and temperature as height changes is seen in Figure 3. Temperatures at .0046 hPa (approximately 84 km) show a similar latitudinal structure: variations in nighttime emission rates and temperature appear to be well correlated. However, temperatures at .0008 hPa have a local minimum at the equator and maxima at mid-latitudes. The cause of this change in correlation is discussed in the modeling section of this paper.

Seasonal variations

The seasonal variation in SABER equatorial OH airglow at two local times is shown in Figure 4. The data are monthly means binned hourly in local time and every 5 degrees in latitude. At 2330 hrs. local time, the variation is semi-annual, with maxima occurring during equinox. At 0530 hrs. local time, no discernible seasonality exists. The variation observed near midnight is similar to AE observations of *Abreu and Yee* [1989] and the SME observations of *Le Texier et al.* [1989] (although the time of SME observations is closer to 0530 hrs., when little seasonal variation is observed by SABER). *Takahashi et al.* [1995] presented ground based observations of OH(9,4) band emission at 3.9°S that showed an approximately 30% variation over the annual cycle, with peaks during March/April and October. Their analysis was of nocturnal means and, considering the local time variation in the annual cycle shown in Figure 4, it is perhaps not surprising the amplitude of the semiannual variation lies somewhere between those observed by SABER. Modeling studies (e.g. *Le Texier et al.*[1987]) have proposed that the semi-annual variation is related to changes in vertical diffusion caused by seasonal changes in gravity wave dissipation. However, it is difficult to reconcile that process with the strong local time variation of the seasonal signal. Given the strong tidal signals present in the emission, it appears likely that the seasonality is instead caused by seasonal changes in the diurnal tide, which is known to have largest amplitude during equinox [*Burrage et al.*, 1995].

Figure 5 shows the emission variation at 60°S, which is clearly annual with a maximum around May. The variation at 60°N (not shown) is very similar, except the cycle is shifted by about 6 months. Unlike the equatorial case, the seasonality is the same for both local times. This seasonality has been observed before [e.g. *Zaragoza et al.* 2001]. It is consistent with transport by the downward component of the mean meridional circulation, which brings air rich in atomic oxygen from the lower thermosphere into the mesopause region during wintertime. As mentioned in the Introduction, the rate of production of excited OH is proportional to the atomic oxygen concentration, and so an enhancement in wintertime emissions is also expected.

Model Simulations

ROSE is a three-dimensional chemical transport model described in *Smith and Ortland* [2001], *Marsh et al.* [2001, 2003], and *Smith and Marsh* [2005]. Model chemistry solves for 27 species and has 101 gas-phase reactions that include those most relevant to the study of OH Meinel emission.

Model volume emission rates (V) are calculated based on the formulation of *Mlynczak et al.*[1998]. The total emission rate (ergs/cm^3/s) from the 9-7 and 8-6 vibrational bands is,

$$V = E_{97}A_{97}n_9 + E_{86}A_{86}n_8 \tag{4}$$

where A_{ij} and E_{ij} are the spontaneous emission rate coefficients and photon energies for the $i-j$ vibrational transition, and n_i is the population of the ith vibrational level. Given that A_{97} and A_{86} are greater than 100s^{-1}, the life times for the v=9 and v=8 states is short. Therefore, assuming steady state and equating production to loss, vibrational level populations are:

$$n_9 = \frac{f_9 P}{L_9} \tag{5}$$

$$n_8 = \frac{f_8 P + n_9 (A_{98} + k_{98}^{O_2}[O_2] + k_{98}^{N_2}[N_2])}{L_8}. \tag{6}$$

As in *Mlynczak et al.* [1998] f_9 and f_8 are 0.44 and 0.28 respectively. L_9 and L_8 are losses through spontaneous emission, collisionally induced vibrational transitions, and the reaction with atomic oxygen:

$$L_i = A_i + k_i^{O_2}[O_2] + k_i^{N_2}[N_2] + k^O[O] \tag{7}$$

ROSE model simulations are for the middle of the observational period (22 April, 2002). To approximate the effects of binning used in the SABER analysis, simulations for an entire day were averaged in longitude to remove any non-migrating components. Photolysis rates are calculated using the empirical solar flux model of *Woods and Rottman* [2002] calculated with a 10.7 cm flux of 186 10^{-22} W/m^2/Hz, which is the average flux between March 26 and May 19, 2002. Wind, temperature and geopotential height at the lower boundary are adjusted to account for forcing of the diurnal and semi-diurnal tides that occurs in the troposphere.

From previous studies (e.g. *Yee et al.* [1997], *Melo et al.* [1999]) and the SABER observations, it is clear that the migrating diurnal tide is an important source of variability of OH Meinel emission in the tropics. It is therefore important that any simulations incorporate realistic diurnal tidal amplitudes and phases. Since the model does not include a troposphere, migrating diurnal and semi-diurnal tidal forcing at the lower model boundary are taken from the Global Scale Wave Model (GSWM) [*Hagan et al.,* 1999] except that the diurnal tide amplitude has been doubled to give better model data agreement in the mesosphere. A similar scaling was performed in the study of *Roble and Shepherd* [1997] when simulating UARS/WINDII OI(5577Å) observations. Tidal forcing generated within the model domain (e.g. by absorption of solar radiation in the stratosphere) was not scaled. Figure 6 shows a data/model comparison of these amplitudes and phases at the equator and 35°S. Diurnal tidal amplitudes were calculated using a non-linear least squares fit to both model and data. The fitting function included both diurnal and semi-diurnal components. Near the height of peak emission the diurnal tide has an amplitude of approximately 20 K at the equator in both observations and simulations. The model appears to be in good agreement with observed tidal phases at all altitudes; both show vertical wavelengths of between 25 and 30 km in the mesosphere. Calculated semidiurnal amplitudes (not shown) at airglow heights are less than 5K at the equator.

Simulated volume emission rates and temperatures under similar conditions to Figures 2 and 3 are shown in Figures 7 and 8. The model correctly predicts many features seen in the observations, including the height of the emission layer and the narrow equatorial peak in emission rates. However, the magnitude of the emission is less than observed. In particular, the model predicts about half the emission at the equator. It is important to note that the model diurnal tidal amplitude matches that deduced from the 55 days of SABER observations, but the tidal amplitude on any one day may be substantially different. The tides in the model vary significantly from day to day; ground-based observations indicate that tides in the actual atmosphere also have considerable variability. Model simulations presented below illustrate the strong dependence of the magnitude of the OH emission on the diurnal tide. Given that each local time bin contains just a few days of data, model/data differences due to the tidal variability are expected to be present.

The changing relationship between emission rate and temperature is well reproduced in the model (Figure 8), and again the strong tidal signatures in tropical temperatures are echoed in the emissions. At high southern latitudes, where the migrating diurnal tide does not have a large amplitude, both temperatures and emission rates are relatively constant throughout the nighttime.

Figure 9 presents the simulated seasonal variations in Meinel emissions at ∼89 km, which does reproduce those seen in the observations. In particular, the local-time dependence of the semi-annual variation is well represented. Results from two simulations are shown: the solid line is for the standard simulation, and the dashed line is for a simulation with a further doubling of the lower boundary diurnal tidal forcing. For the case with enhanced diurnal tide forcing, the seasonal variation (at 2325 hrs. local time) is more pronounced than the case with the standard forcing. This indicates the amplitude of the semi-annual oscillation seen in observations close to midnight is dependent on the seasonal variation in the diurnal tide. Just as in the observations, emissions at 0515 hrs. are relatively constant throughout the year. It is clear from the phases plotted in Figure 6b that at 0515 hrs. the temperature perturbation due to the migrating diurnal tide is near its minimum. We would expect that the tidal effect on atomic oxygen would also be small at this time, since both temperature and oxygen respond similarly to the vertical component of the tidal wind. Therefore, seasonal variations in tidal amplitudes would have the weakest impact on the emissions at around 0500 hrs. and 1700 hrs. This appears to be the case for both observations and simulations. At high-latitudes there is little variation in the date and amplitude of the annual maximum emission; peak emission occurs during May/June at both local times. Again, here we expect no local time dependence because the tidal amplitudes are low. During summertime, low emission rates seen at 0515 hrs. local time are due to the large reduction in emission during the daytime.

Discussion

Figures 10 and 11 show the local time variability in OH Meinel emission as simulated by the ROSE model at the equator and 57.5°S. Data from two simulations are shown; the standard model, and one in which the diurnal and semidiurnal tides are eliminated. The tides are removed by zonally averaging the solar and chemical heating rates within the model domain and zeroing the GSWM tidal forcing at the lower boundary. Observed volume emission rates and temperatures are also shown for comparison. At the equator the model emission rates are lower than observed and the observed temperature diurnal maximum is not well represented. The agreement at 57.5°S is better, and indicates that deficiencies in the model are more likely a result of reproducing tidal fields for the observational period, than any missing chemical mechanism.

It is clear from the simulations that the diurnal tide dramatically affects the nighttime emission rates. At 84 km the emission rate at midnight is decreased by about a factor of three in the run without the diurnal and semi-diurnal tide. In both cases, at 84 and 88 km, the nighttime emission follows the variation in atomic oxygen, which is to be expected from (3). The decrease in emission throughout the night at 84 km in the 'no-tide' case can be explained as follows. After sunset, the photolytic sources of atomic oxygen cease to exist, and oxygen is primarily lost in reactions with molecular oxygen, ozone, and OH. The lifetime for this loss (τ) is:

$$\tau = \left(k_{O+O_2+M} * O_2 * M + k_{O+O_3} * O_3 + k_{O+OH} * OH\right)^{-1} . \tag{8}$$

During the night, τ is about 6 hrs. at 84 km, a day at 88 km, and 2 months at 102 km. In the absence of advection and diffusion, atomic oxygen decreases throughout the night; the rate of decrease is larger at lower altitudes as a consequence of higher OH, O_2, and total densities. Since OH Meinel emission is proportional to atomic oxygen, it should also decrease throughout the night. The dotted line in Figure 10 represents the expected drop-off in emission that might be expected if the atomic oxygen concentration depended only on chemistry, i.e.

$$V(t) = V_0 exp(-t/\tau(t)), \tag{9}$$

where V_0 is the emission rate shortly after sunset. The increase in lifetimes with height is clear from the slopes of the dotted lines of Figure 10.

This assumption fits the 'no-tide' case reasonably well, with differences likely arising from the presence of other wave perturbations or gravity-wave induced vertical diffusion. It also fits the diurnal variation at 57.5°S shown in Figure 11, where the standard and 'no-tide' case are quite similar. However, the large increases in emission rates during the night seen in both model and observations at the equator obviously do not fit this simple model. Emissions are predominantly responding to atomic oxygen concentrations, which are increasing in spite of the absence of a photochemical source. The fact that temperatures are also increasing implies the source is dynamical and is a result of vertical advection; a downward wind will tend to increase temperatures through adiabatic heating and also increase atomic oxygen since its mixing ratio increases rapidly with height.

At 102 km nighttime emission rates are still enhanced compared to the 'no-tide' simulation; the same as at 88 km. However, at the higher altitude both atomic oxygen and temperature are substantially lower relative to the 'no-tide' simulation. This change can be understood by referring to equations (2) and (3). We can re-write the production of excited OH as:

$$P = k_{O+O_2+M}[O][O_2][M]. \tag{10}$$

The reaction rate constant $= k_{O+O_2+M}$ has a value of $6.0 \times 10^{-34}(300/T)^{2.4}$, and so tidally induced adiabatic cooling will increase the production of excited OH. In addition, on a constant pressure surface, a decrease in temperature will increase the total number density, and so increase the rate of the three-body recombination reaction. The combination of temperature and density effects is enough to counteract the decrease in atomic oxygen, and still results in increased emission relative to the case without tidal advection. In general, temperature and density changes from vertical motions affect OH Meinel emissions in opposition to atomic oxygen changes. The height dependence of the relative amplitudes of these effects at a particular time in the diurnal cycle is shown Table 1. At the lowest and highest altitudes, tides tend to increase OH emissions. The tidally induced atomic oxygen mixing ration change alone would be enough to increase emissions by 50% at 88 km (around the emission peak). However, density and temperature changes reduce this effect to around 22%. In contrast, at 99 km, the reduction in oxygen alone would reduce emissions by 36%, but the combined tidal effect is an increase in emission of 11%. The cause of changing emisison/temperature correlations seen in Figure 3 is now clear. At lower altitudes the equatorial enhancement in emission results from advection of atomic oxygen. The simultaneous increase in temperature is an additional response to vertical motions, but does not lead to an emission enhancement (in fact the opposite is true). In contrast, at higher altitudes, the equatorial emission increase is a direct consequence of temperature changes and associated changes in total density density.

Summary

This paper has investigated the variability of OH Meinel airglow observed by the TIMED/SABER instrument. Although the OH emission has been observed for several decades from the ground and from space, its global variability over diurnal and seasonal time scales has not been previously characterized and explained. Observations of this emission are valuable for several reasons: it responds to perturbations by waves and tides in the mesosphere; it provides a reliable technique for determining atomic oxygen, which is difficult to determine by other means; and it can be used for determining the chemical heating rate from the most important exothermic reaction in the mesosphere [*Mlynczak et al.,* 2000].

Comparisons of the SABER observations with a 3-dimensional chemical transport model show that much of the variability in emissions is caused by variations in the production rate of ozone ($k_{O+O_2+M}[O][O_2][M]$). At the height of peak emission, variations are predominantly caused by changes in atomic oxygen resulting from vertical transport. Above the emission layer peak, emission variations are driven by changes in temperature and density again caused by vertical transport. The differing causes manifest themselves as opposite signs in the correlations between emission and temperature. The correlation is positive where O transport is the dominant process (coinciding with the sharp vertical gradient in nighttime oxygen density in the middle to upper mesosphere) and negative where changes in the density and reaction rates are more important.

It appears that the diurnal migrating tide has a considerable effect on equatorial emissions, and is the predominant cause of the diurnal and seasonal variations in low latitudes. The observed semi-annual variation in emission is a result of the seasonal change in tidal amplitudes, and is not caused by changes in diffusive transport as was previously proposed. Interestingly, the same diffusive mechanism was used to explain variations in mesospheric ozone [*Garcia and Solomon*, 1985], since both ozone and OH emission depend critically on the distribution of atomic oxygen. More recently it was suggested that tides could play an important role in mesospheric ozone variability [*Mlynczak et al.,* 2000; *Marsh et al.,* 2002]. It follows that the topic of ozone variability should also be revisited using SABER observations and 3-dimensional models.

Acknowledgments. Support for this work was provided by NASA Office of Space Science. The National Center for Atmospheric Research is operated by the University Corporation for Atmospheric Research under sponsorship of the National Science Foundation.

References

Abreu, V.J., and J.-H. Yee (1989), Diurnal and seasonal variation of the nighttime OH (8-3) emission at low latitudes, *J. Geophys. Res.,* 94, 11949-11957.

Burrage, M.D., M.E. Hagan, W.R. Skinner, D.L. Wu, and P.B. Hays (1995), Long-term variability in the solar diurnal tide observed by HRDI and simulated by the GSWM, *Geophys. Res. Lett.,* 22, 2641-2644.

Forbes, J.M. (1982), Atmospheric Tides .1. Model Description and Results for the Solar Diurnal Component, *J. Geophys. Res.,* 87, 5222-5240.

Garcia, R.R., and S. Solomon (1985), The effect of breaking gravity waves on the dynamics and chemical composition of the mesosphere and lower thermosphere, *J. Geophys. Res.,* 90(D2), 3850-3868.

Hagan, M.E., M. D. Burrage, J. M. Forbes, J. Hackney, W. J. Randel, and X. Zhang (1999), GSWM-98: Results for migrating solar tides, *J. Geophys. Res.,* 104, 6813-6827.

Hecht, J.H., R.L. Walterscheid, R.G. Roble, R.S. Lieberman, E.R. Talaat, S.K. Howat, R.P. Lowe, D.N. Turnbull, C.S. Gardner, R. States, P.D. Dao (1998), A comparison of atmospheric tides inferred from observations at the mesopause during ALOHA-93 with the model predictions of the TIME-GCM, *J. Geophys. Res.,* 103(D6), 6307-6321.

Le Texier, H, S. Solomon, and R.R. Garcia (1987), Seasonal variability of the OH Meinel bands, *Planet. Space Sci.*, 35, 977-989.

Le Texier, H, S. Solomon, R. J. Thomas, and R.R. Garcia (1989), OH* (7-5) Meinel band dayglow and nightglow measured by the SME limb scanning near-infrared spectrometer: comparison of the observed seasonal variability with two-dimensional model simulations, Annales Geophysicae, 7, 365-374.

Lowe, R.P., L.M. LeBlanc, K.L. Gilbert (1996), WINDII/UARS observation of twilight behaviour of the hydroxyl airglow, at mid-latitude equinox, Journal of Atmospheric and Terrestrial Physics, 58(16), 1862-1869.

Marsh, D.R., A.K. Smith, G.P. Brasseur, M. Kaufmann, and K.U. Grossmann (2001), The existence of a tertiary ozone maximum in the high-latitude middle mesosphere, *Geophys. Res. Lett.,* 28, 4531-45534.

Marsh, D. R., W. R. Skinner, A. R. Marshall, P. B. Hays, D. A. Ortland, and J. Yee (2002), High Resolution Doppler Imager observations of ozone in the mesosphere and lower thermosphere, *J. Geophys. Res.,* , 107(D19), 4390, doi:10.1029/2001JD001505.

Marsh, D.R., A.K. Smith, and E. Noble, Mesospheric ozone response to changes in water vapor (2003), *J. Geophys. Res.,* , 108(D3), 4109, doi:10.1029/2002JD002705.

Melo, S.M.L., R.P. Lowe, H. Takahashi (1999), The nocturnal behavior of the hydroxyl airglow at the equatorial and low latitudes as observed by WINDII: comparison with ground-based measurements, *J. Geophys. Res.,* 104, 24657-24665.

Melo, S. M. L., R. P. Lowe, and J. P. Russell (2000), Double-peaked hydroxyl airglow profiles observed from WINDII/UARS, *J. Geophys. Res.,* 105, 12,397-12,404.

Mertens, Christopher J., et al. (2004), SABER observations of mesospheric temperatures and comparisons with falling sphere measurements taken during the 2002 summer MaCWAVE campaign, *Geophys. Res. Lett.,* 31, L03105, doi:10.1029/2003GL018605.

Mertens, C. J., III (2001), Retrieval of mesospheric and lower thermospheric kinetic temperature from measurements of CO2 15 μm earth limb emission under non-LTE conditions, *Geophys. Res. Lett.,* 28, 1391-1394.

Mlynczak, M.G. (1997), Energetics of the mesosphere and lower thermosphere and the SABER experiment, *Adv. Space Res.*, 20(6), 1177-1183.

Mlynczak, M. G., D. K. Zhou, and S. M. Adler-Golden (1998), Kinetic and spectroscopic requirements for the inference of chemical heating rates and atomic hydrogen densities from OH Meinel band measurements, *Geophys. Res. Lett.,* 25(5), 647-650.

Mlynczak, M. G., R.R. Garcia, R.G. Roble and M. Hagan (2000), Solar energy deposition rates in the mesosphere derived from airglow measurements: Implications for the ozone model deficit problem, *J. Geophys. Res.,* 105, 17527-17538.

Pendleton, W.R. Jr., M.J. Taylor, and L.C. Gardner, (2000) Terdiurnal oscillations in OH Meinel rotational temperatures for fall conditions at northern mid-latitude sites, *Geophys. Res. Lett.,* 27, 1799-1802.

Phillips, F. G.B. Burns, W.J.R. French, P.F.B. Williams, A.R. Klekociuk, and R.P. Lowe, (2004) Determining rotational temperatures from the OH(8-3) band, and a comparison with OH(6-2) rotational temperatures at Davis, Antarctica, *Ann. Geophys.* 22, 1549-1561.

Roble, R. G., and G. G. Shepherd (1997), An analysis of wind imaging interferometer observations of O(1S) equatorial emission rates using the thermosphere-ionosphere-mesosphere-electrodynamics general circulation model, *J. Geophys. Res.,* , 102(A2), 2467-2474.

Smith, A.K., and D.A. Ortland (2001), Modeling and analysis of the structure and generation of the terdiurnal tide, *J. Atmos. Sci.*, 58, 3116-3134.

Smith, A.K., and D.R. Marsh (2005), Processes that account for the ozone maximum at the mesopause, *J. Geophys. Res.,* , in press.

Takahashi, H., B.R. Clemesha, and P.P. Batista (1995), Predominant semi-annual oscillation of the upper mesospheric airglow intensities and temperatures in the equatorial region, *J. Atmos. Terr. Phys.*, 57(4), 407-414.

Taylor, M. J., W. R. Pendleton Jr., S. Clark, H. Takahashi, D. Gobbi, and R. A. Goldberg (1997), Image measurements of short-period gravity waves at equatorial latitudes, *J. Geophys. Res.,* 102(D22), 26,283-26,300.

Ward, W. E., J. Oberheide, M. Riese, P. Preusse, and D. Offermann (1999), Tidal signatures in temperature data from CRISTA 1 mission, *J. Geophys. Res.,* , 104, 16,391-16,404.

Woods, T.N., and G.J. Rottman (2002), Solar ultraviolet variability over time periods of aeronomic interest, in Comparative Aeronomy in the Solar System, ed. M, Mendillo, A. Nagy, and M. Stefanis, Geophys. Monogr., 130, pp. 221-234, doi: 10.1029/130GM14.

Yee, J., G. Crowley, R. G. Roble, W. R. Skinner, M. D. Burrage, and P. B. Hays (1997), Global simulations and observations of O(1S), O2($^1\Sigma$) and OH mesospheric nightglow emissions, *J. Geophys. Res.,* 102, 19,949-19,968.

Yudin, V. A., M. A. Geller, B. V. Khattatov, D. A. Ortland, M. D. Burrage, C. McLandress, and G. G. Shepherd (1998), TMTM simulations of tides: Comparison with UARS observations, *Geophys. Res. Lett.,* 25(2), 221-224.

Zaragoza, G. (2001), The nocturnal behavior of the hydroxyl layer as observed by ISAMS/UARS, *Adv. Space Res.*, 27, 1691-1696.

Zaragoza, G., F. W. Taylor, and M. Lopez-Puertas (2001), Latitudinal and longitudinal behavior of the mesospheric OH nightglow layer as observed by the Improved Stratospheric and Mesospheric Sounder on UARS, *J. Geophys. Res.,* 106, 8027-8034.

D.R. Marsh, A.K. Smith, Atmospheric Chemistry Division, National Center for Atmospheric Research, P.O. Box 3000, Boulder, CO 80307-3000. (email:

marsh@ucar.edu, aksmith@ucar.edu)

Received ____________________

Table 1. Relative effects on equatorial OH Meinel volume emission rates of tidal perturbations at the specific local time of 0130 LT. V' is tidally perturbed emission rate (1e7 ergs/cm^3/s). Ratios give the emission in the presence of tides relative to a simulation with tidal perturbations removed: $\frac{V'}{V}$ is the net impact; $\frac{V(O')}{V(O)}$ is the impact due to O changes; $\frac{V(n')}{V(n)}$ is the impact due to background density changes; and $\frac{V(T')}{V(T)}$ is the impact due to temperature dependent reaction rate changes.

z(km)	V'	$\frac{V'}{V}$	$\frac{V(O')}{V(O)}$	$\frac{V(n')}{V(n)}$	$\frac{V(T')}{V(T)}$
102.90	0.17	1.41	0.65	1.38	1.32
98.70	0.39	1.11	0.64	1.28	1.25
96.60	0.54	1.03	0.68	1.20	1.19
92.40	0.90	0.97	0.87	1.05	1.05
88.20	1.07	1.22	1.50	0.91	0.91
84.00	0.67	3.50	5.04	0.85	0.83

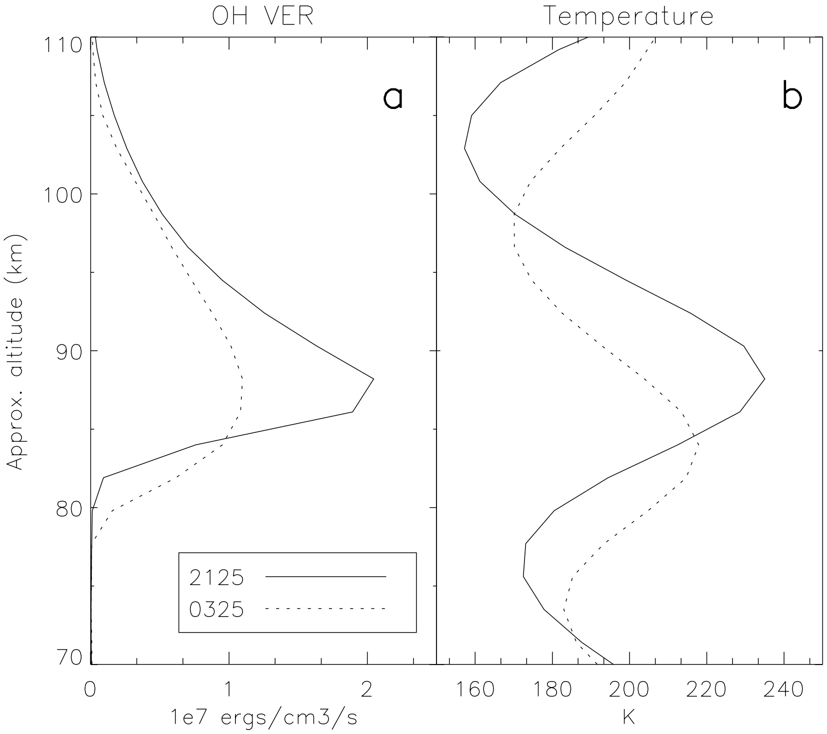

Figure 1. Sample average SABER profiles at 2.5°N for a) OH Meinel airglow (2.0μm), and b) temperature. Profiles are shown for 2125 hrs. local time (solid lines) and 0325 hrs. local time (dashed lines).

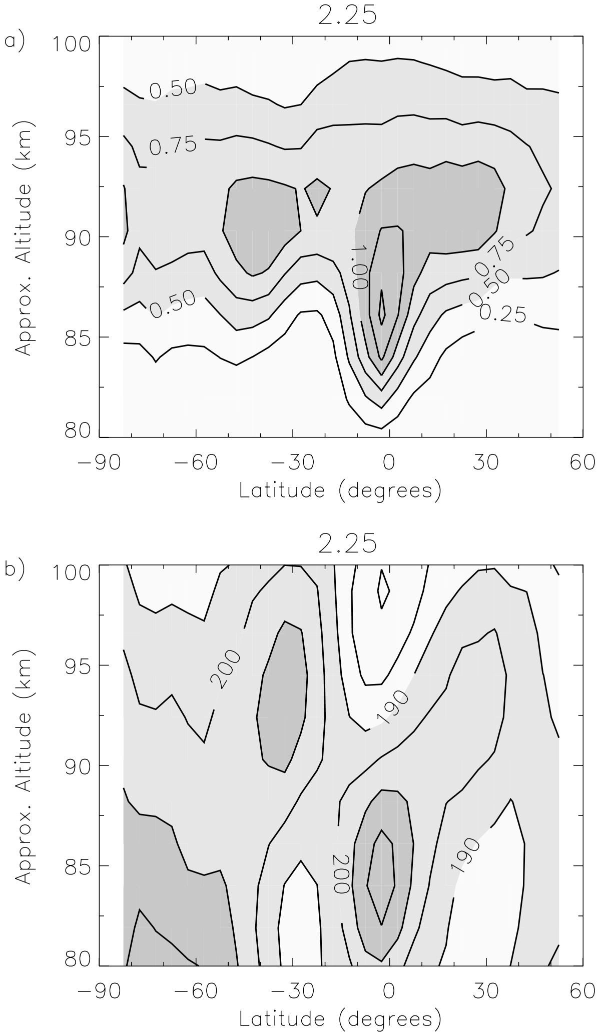

Figure 2. a) SABER OH Meinel 2.0μm volume emission rates (1e7 ergs/cm^3/s) at 0215 hrs. local time averaged over the period March 26 to May 19, 2002. b) SABER mean temperatures for the same period.

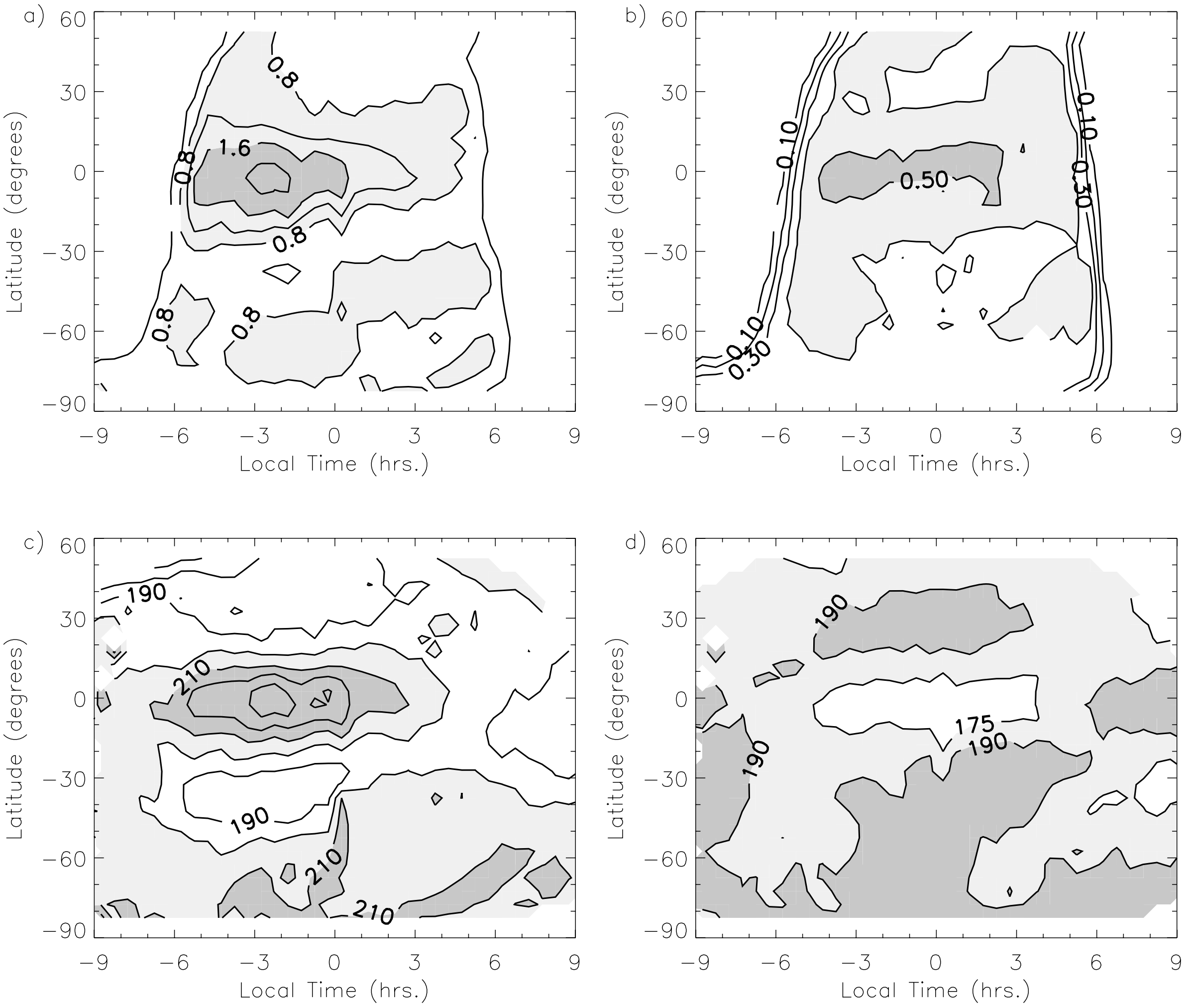

Figure 3. SABER OH Meinel VER (1e7 ergs/cm^3/s) on pressure surfaces a) ≈88km and b) ≈99km. Observed temperature on pressure surfaces c) ≈88km and d) ≈99km. Data from the same period as Figure 2

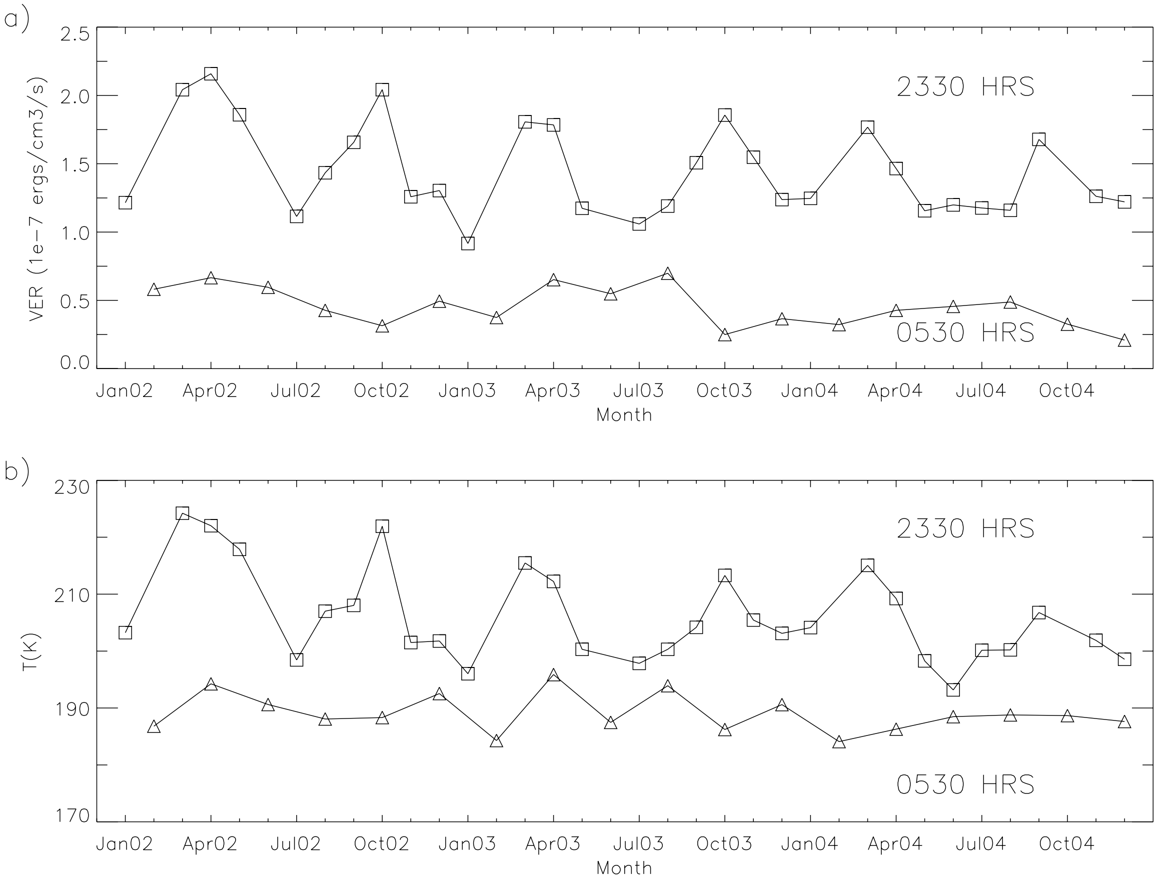

Figure 4. Observed seasonal variation in a) OH Meinel emission rate and b) temperature at 0.0032 hPa (≈89 km) for latitudes within 7.5° of the equator. Data are monthly means of all observations that fell with 30 minutes of 2330 hrs. (squares) and 0530 hrs. (triangles) local time.

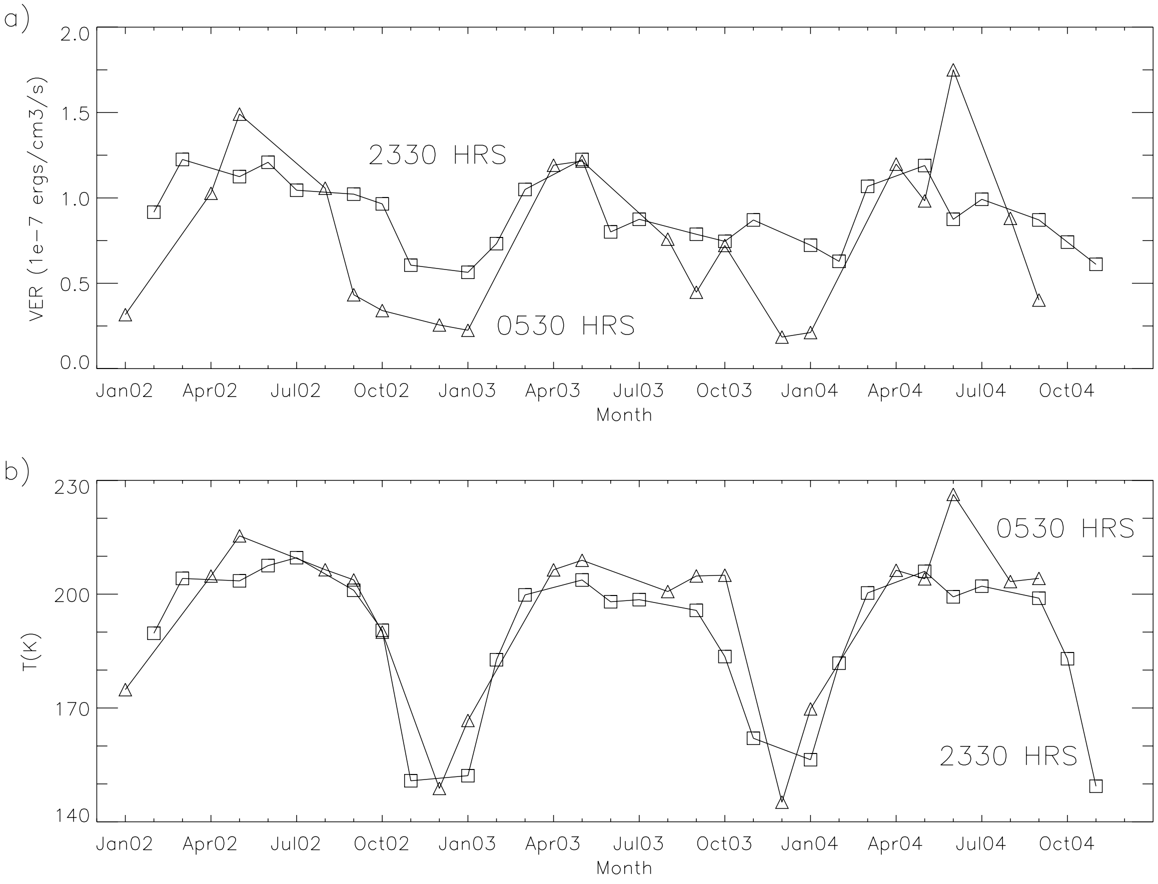

Figure 5. As in Figure 4 but at 60°S.

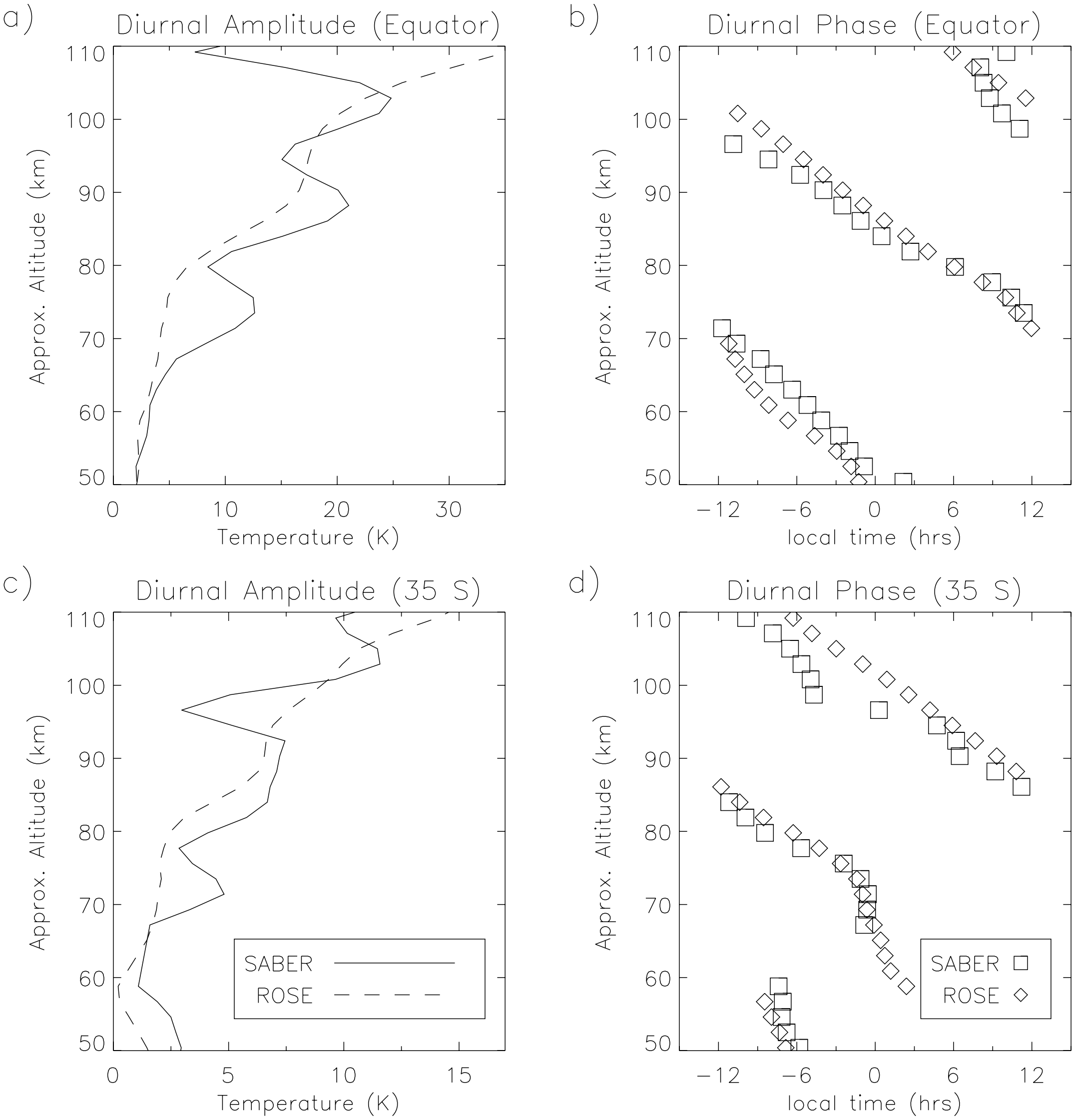

Figure 6. Amplitude and phase of the migrating diurnal tide in temperature at the equator (a)-(b), and 35°S latitude. Estimates based on SABER observations (solid line and squares) over the same period as Figure 2. ROSE results (dashed line and diamonds) are for 22 April, 2002.

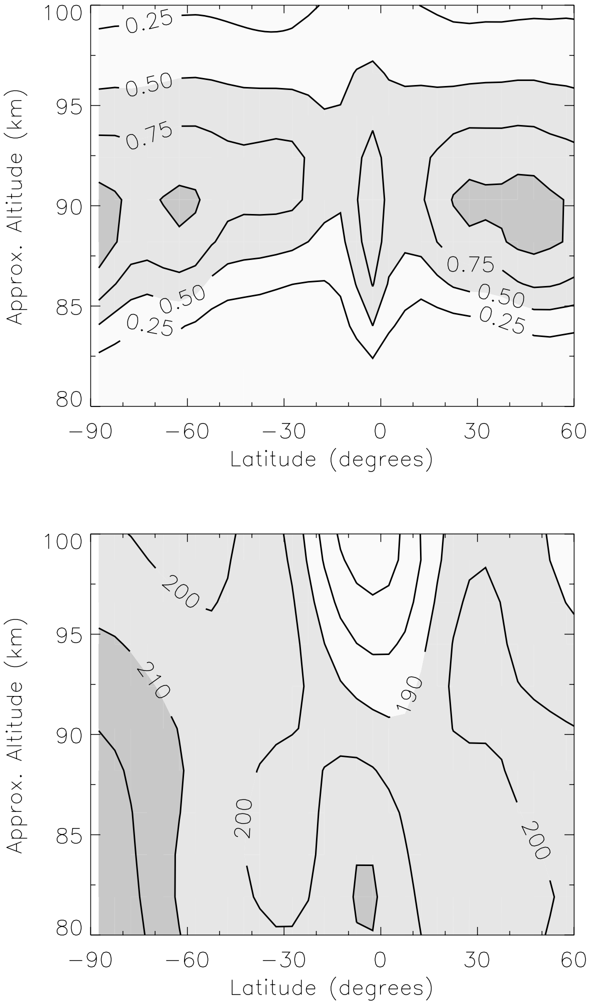

Figure 7. ROSE simulations of latitude/height distribution of a) OH Meinel emission (1e7 ergs/cm^3/s) and b) temperature (K) at 0315 hrs. local time on 22 April, 2002.

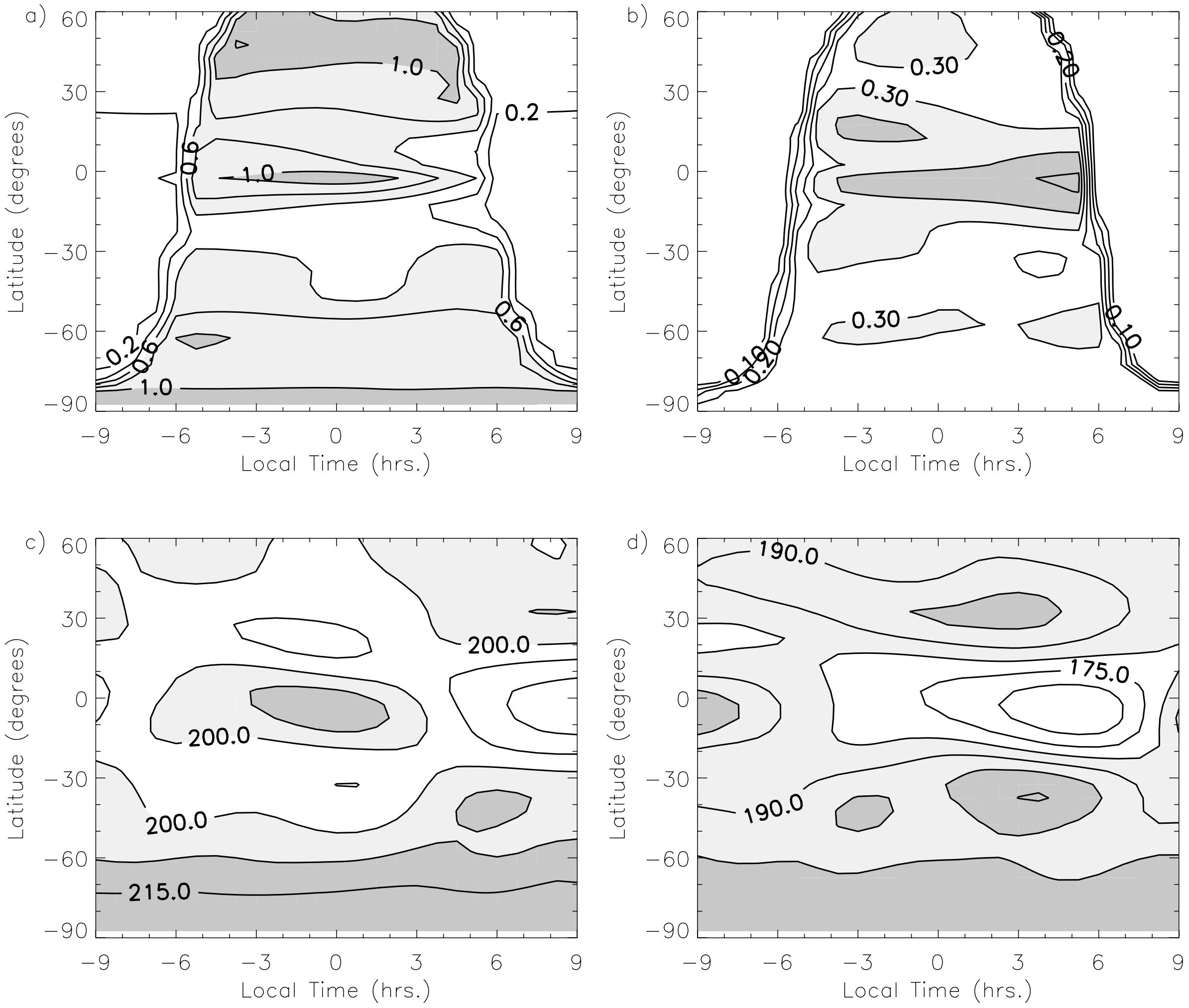

Figure 8. ROSE simulations of OH Meinel emission (1e7 ergs/cm^3/s) and temperature (K) at ≈88 km (a,c) and ≈99 km (b,d) on 22 April, 2002.

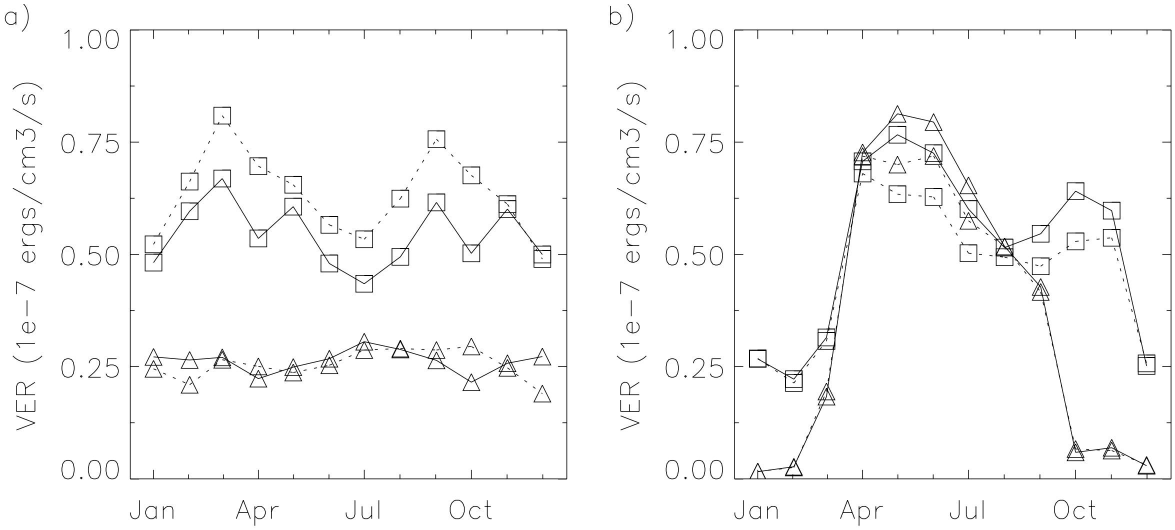

Figure 9. Modeled seasonal variation in OH Meinel emission rate at 0.0032 hPa. a) Variation at the equator at 2325 hrs. local time (squares) and 0515 hrs. local time (triangles). b) As in a) but at 60°S. Solid line is for standard simulation, dotted line is for run with increased lower boundary tidal forcing.

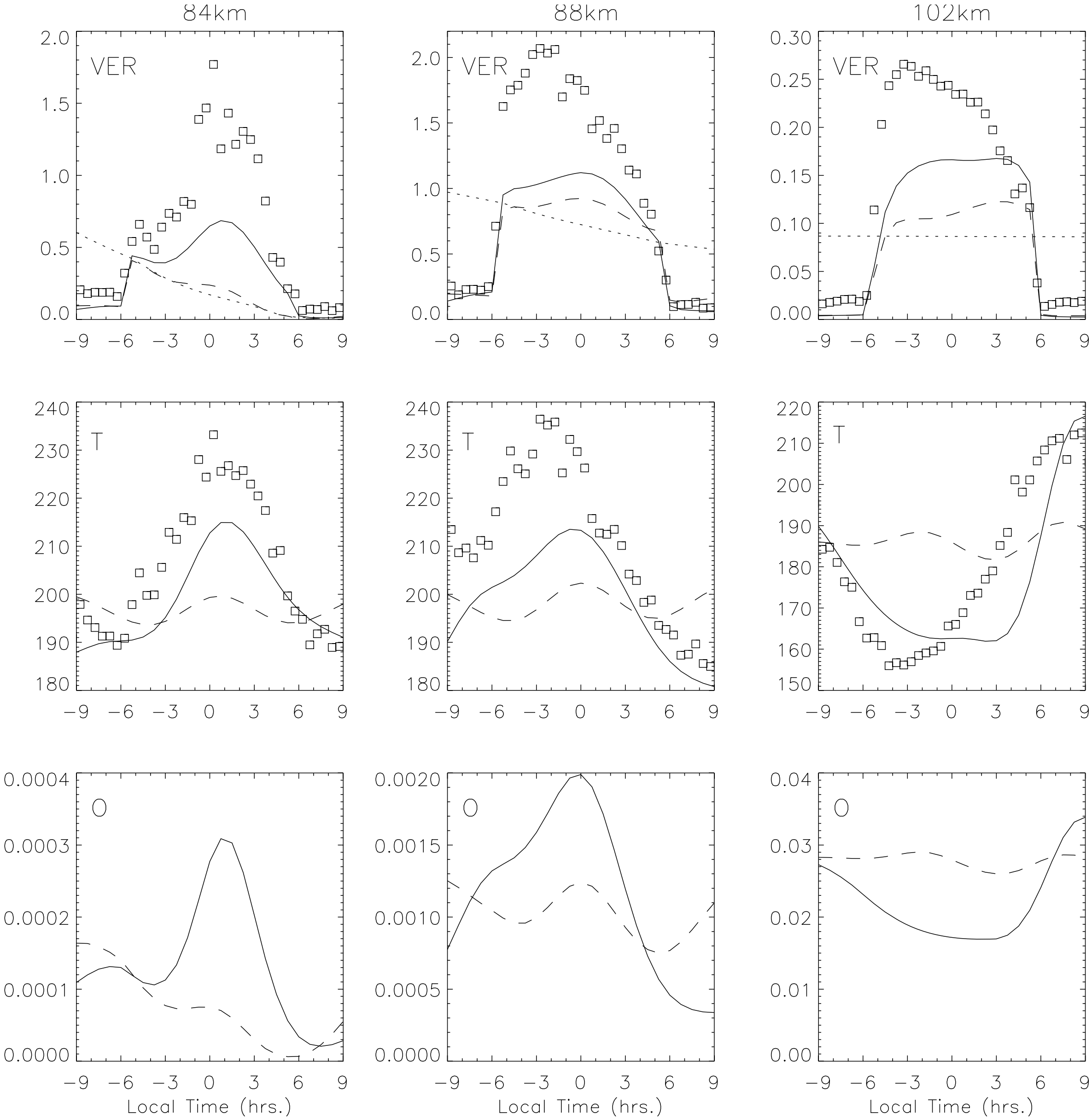

Figure 10. (top) Simulated nocturnal variation in equatorial OH Meinel emission at three different altitudes. Solid line is standard simulation, and dashed line is for simulation without the diurnal and semi-diurnal tides. Dotted line represents expected drop in nighttime emission due only to chemical losses in atomic oxygen. Simultaneous temperature (middle) and atomic oxygen (bottom) variations are also shown. SABER observations are shown for comparison (squares).

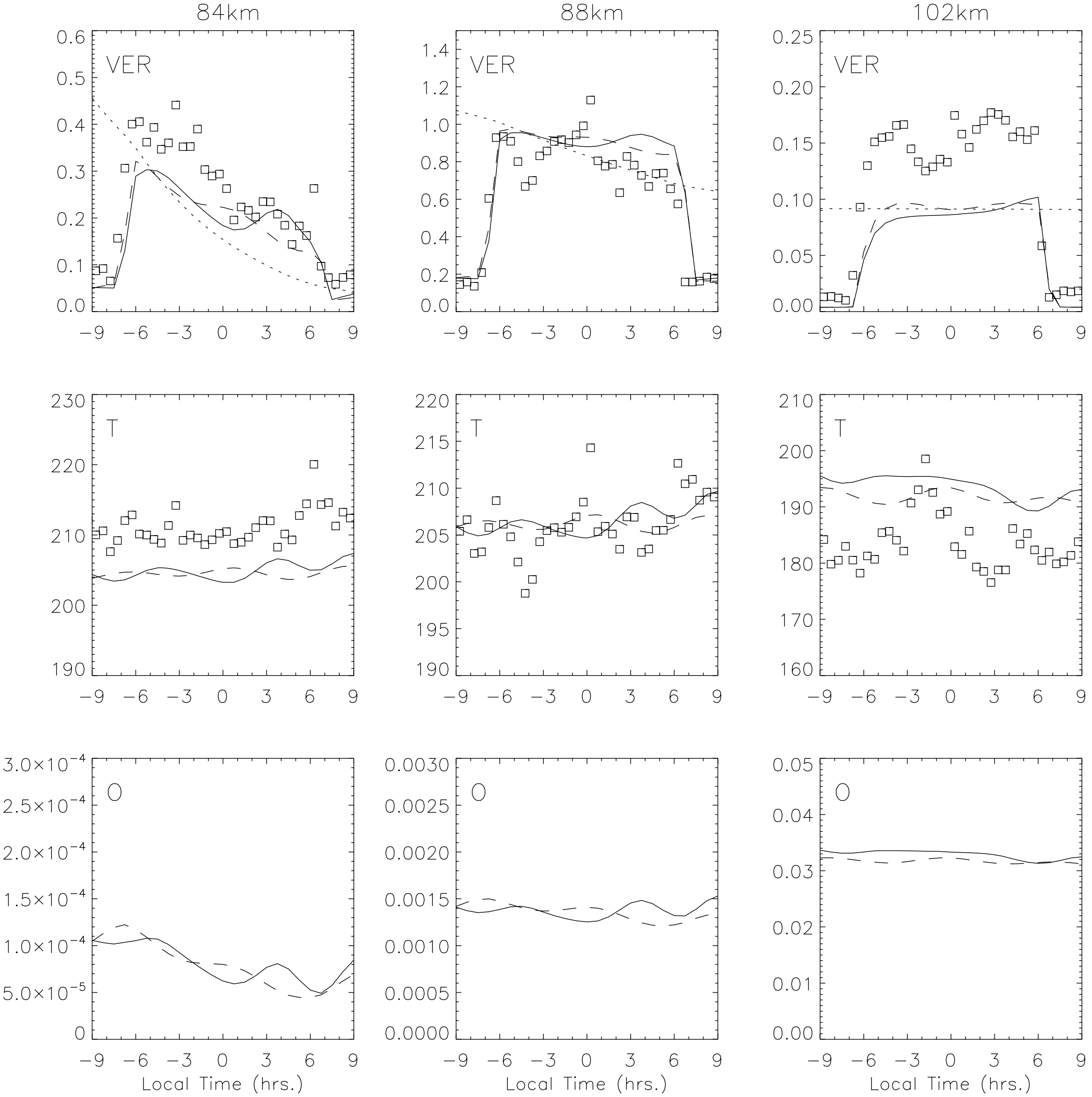

Figure 11. As Figure 10 for 57.5°S.